The Cryosphere Discuss., 8, 2995–3035, 2014
www.the-cryosphere-discuss.net/8/2995/2014/
doi:10.5194/tcd-8-2995-2014

The Cryosphere Discussions
Open Access

Simultaneous solution for mass trends on the West Antarctic Ice Sheet

N. Schön[1], A. Zammit-Mangion[1,2], J. L. Bamber[1], J. Rougier[2], T. Flament[3], F. Rémy[4], and S. B. Luthcke[5]

[1]Bristol Glaciology Centre, School of Geographical Sciences, University of Bristol, Bristol, UK
[2]Department of Mathematics, University of Bristol, Bristol, UK
[3]School of Earth and Environment, University of Leeds, Leeds, UK
[4]LEGOS, Toulouse, France
[5]NASA, Greenbelt, MD, USA

Received: 11 April 2014 – Accepted: 8 May 2014 – Published: 5 June 2014

Correspondence to: J. L. Bamber (j.bamber@bristol.ac.uk)

Published by Copernicus Publications on behalf of the European Geosciences Union.

Abstract

The Antarctic Ice Sheet is the largest potential source of future sea-level rise. Mass loss has been increasing over the last two decades in the West Antarctic Ice Sheet (WAIS), but with significant discrepancies between estimates, especially for the Antarctic Peninsula. Most of these estimates utilise geophysical models to explicitly correct the observations for (unobserved) processes. Systematic errors in these models introduce biases in the results which are difficult to quantify. In this study, we provide a statistically rigorous, error-bounded trend estimate of ice mass loss over the WAIS from 2003–2009 which is almost entirely data-driven. Using altimetry, gravimetry, and GPS data in a hierarchical Bayesian framework, we derive spatial fields for ice mass change, surface mass balance, and glacial isostatic adjustment (GIA) without relying explicitly on forward models. The approach we use separates mass and height change contributions from different processes, reproducing spatial features found in, for example, regional climate and GIA forward models, and provides an independent estimate, which can be used to validate and test the models. In addition, full spatial error estimates are derived for each field. The mass loss estimates we obtain are smaller than some recent results, with a time-averaged mean rate of $-76 \pm 15\,\mathrm{GT\,yr^{-1}}$ for the WAIS and Antarctic Peninsula (AP), including the major Antarctic Islands. The GIA estimate compares very well with results obtained from recent forward models (IJ05-R2) and inversion methods (AGE-1). Due to its computational efficiency, the method is sufficiently scalable to include the whole of Antarctica, can be adapted for other ice sheets and can easily be adapted to assimilate data from other sources such as ice cores, accumulation radar data and other measurements that contain information about any of the processes that are solved for.

TCD
8, 2995–3035, 2014

1 Introduction

Changes in mass balance of the Antarctic ice sheet have profound implications on sea level. While there is a general consensus that West Antarctica has experienced ice loss over the past two decades, the range of mass-balance estimates still differs significantly (compare, e.g, Shepherd et al., 2012, with Gunter et al., 2014). Studies typically make use of satellite altimetry (Shepherd et al., 2012), satellite gravimetry (Chen et al., 2006; King et al., 2012; Sasgen et al., 2013; Luthcke et al., 2013), or a combination of satellite and climate model simulations (Rignot et al., 2011) to provide estimates. In the latter case, the balance is found by deducting output ice flux from input snowfall in a technique sometimes referred to as the Input-Output Method (IOM).

Different approaches have different sources of error. The dominant error in the gravimetry-based estimates is a result of incomplete knowledge on glacial isostatic adjustment (GIA), which constitutes a significant proportion of the mass-change signal (Velicogna and Wahr, 2006). For satellite altimetry, uncertainties arise from incomplete knowledge of the temporal variability in precipitation (Lenaerts et al., 2012; Frezzotti et al., 2012), and the compaction rates of firn (Arthern, 2010; Ligtenberg, 2011): quantities which play a central role in determining the density of the observed volume change. For the IOM, the main sources of errors stem from the surface mass balance (SMB) profiles used (obtained from a regional climate model), and uncertainties in the ice discharge map. Recent improvements in regional climate modelling have reduced the uncertainty in the SMB component but differences between estimates for the Antarctic ice sheet as a whole still exceed recent estimates of its mass imbalance (Van de Berg et al., 2006; King et al., 2012).

To minimize the dependency on forward models, recent studies have combined altimetry and GRACE to obtain a data-driven estimate of GIA and ice loss simultaneously (Riva et al., 2009; Gunter et al., 2014). Here, we aim to provide a model-independent estimate not only of GIA, but also of the SMB, firn compaction rates and of the mass loss/gain due to ice dynamics (henceforward simply referred to as ice dynamics). In

TCD
8, 2995–3035, 2014

doing so, we eliminate the dependency of the solution on solid-Earth and climate models. The trends for ice dynamics, SMB, GIA, and firn compaction are obtained independently through simultaneous inference in a hierarchical statistical framework. The climate and firn compaction models are used solely to provide prior information about the spatial smoothness of the SMB-related processes. Systematic biases in the models have, therefore, minimal impact on the solutions. In addition, we employ GPS bedrock uplift rates to further constrain the GIA signal. In future work the GPS data will also be used to constrain localised ice mass trends that cause an instantaneous elastic response of the lithosphere (Thomas and King, 2011). The statistical framework uses expert knowledge about smoothness properties of the different processes observed (i.e. their spatial and temporal variability) and provides statistically sound regional error estimates that take into account the uncertainties in the different observation techniques. The study reported here was performed as a proof-of-concept for a time-evolving version of the framework for the whole Antarctic ice sheet, which is currently under development.

The paper is organised as follows. In Sect. 2 we describe both the observation data and auxiliary data sets used while in Sect. 3 we give a summary of the statistical methodology employed (full details can be found in Zammit-Mangion et al., 2013). Section 4 outlines the main results and is followed by a discussion in Sect. 5. Section 6 concludes the work.

2 Data

In this section we describe the data employed which is divided into two groups. The first group contains observational data which play a direct role in providing mass balance estimates. These include satellite altimetry, satellite gravimetry and GPS data (Sects. 2.1–2.3). The second group contains auxiliary data (both observational and data extracted from geophysical models), which we use to aid the assimilation implicitly. These are discussed in Sect. 2.4.

TCD
8, 2995–3035, 2014

2.1 Altimetry

We make use of two altimetry data sets in this study, obtained from the Ice, Cloud and land Elevation Satellite (ICESat) and the Environment Satellite (EnviSat).

ICESat: in this study, we used ICESat elevation rates ($\mathrm{d}h/\mathrm{d}t$) based on release 33 data from February 2003 until October 2009 (Zwally et al., 2011). The data includes the "86S" inter-campaign bias correction presented in Hofton et al. (2013) and the centroid Gaussian correction (Borsa et al., 2014) made available by the National Snow and Ice Data Centre (NSIDC). Pre-processing was carried out as described in Sørensen et al. (2011). Since ICESat tracks do not precisely overlap, a regression approach was used for trend extraction, in which both spatial slope (both across-track and along-track) and temporal slope ($\mathrm{d}h/\mathrm{d}t$) were simultaneously estimated (Howat et al., 2008; Moholdt et al., 2010). A regression was only performed if the area under consideration, typically 700 m long and a few hundred metres wide, had at least 10 points from four different tracks that span at least a year. Regression was carried out twice, first to detect outliers (data points which lay outside the 2σ confidence interval), and second to provide a trend estimate following outlier omission. The standard error on the regression coefficient (in this case $\mathrm{d}h/\mathrm{d}t$), $\mathrm{SE}_{\mathrm{coef}}$, was calculated through (Yan, 2009):

$$\mathrm{SE}_{\mathrm{coef}} = \frac{1}{\sqrt{n-2}} \sqrt{\frac{\sum_i e_i^2}{\sum_i (x_i - \bar{x})^2}} \tag{1}$$

where $\boldsymbol{e} = [e_i]$ is the vector of residuals, n is the sample size, and $\boldsymbol{x} = [x_i]$ is the input with mean $\bar{x}$. It should be noted that this standard error is not equivalent to the measurement error, but takes into account sample size, as well as the variance of both input data and residuals of the regression. Only elevation changes with an associated standard error on $\mathrm{d}h/\mathrm{d}t$ of less than $0.40\,\mathrm{m\,yr^{-1}}$ were considered. The $0.40\,\mathrm{m\,yr^{-1}}$ threshold was selected by trial and error to avoid a noisy spatial pattern of points that are close together and opposite in sign, usually because the regression is based on

TCD
8, 2995–3035, 2014

a small subset of overpasses. Data above the latitude limit of 86° S were omitted. The remaining data were gridded on a polar-stereographic projection (central latitude 71° S; central longitude 0° W, and origin at the South Pole), at a 1 km resolution and then averaged over a 20 km grid. The error used in the modelling framework was then the spread (standard deviation) of the trends within each 20 km grid box, as in Riva et al. (2009).

EnviSat: the EnviSat mission began in September 2002 and ended in November 2010. Compared to laser altimetry, radar altimetry is less suited for measurements over ice for several well-known reasons: the large spatial footprint, the poor performance in steeper-sloping marginal areas (Thomas et al., 2008), and the snow-pack radar penetration (Zwally and Brenner, 2001). On the other hand EnviSat data exhibit better temporal and spatial coverage. We use the EnviSat altimetry along-track trends presented in Flament et al. (2012), which were obtained by binning all points within a 500 m radius and then fitting a 10-parameter least-squares model in order to correct for across-track topography and changes in snowpack properties. The re-trended residuals were then used to obtain linear trends over the 2003–2009 ICESat period for our study. As with ICESat, the data were averaged over a 20 km grid and the standard deviation of the trends were used as the error at this scale.

2.2 GRACE

The Gravity Recovery and Climate Experiment (GRACE, Tapley et al., 2005) has provided temporally continuous gravity field data since 2002. Different methods have been used to provide mass change anomalies from the Level 1 data. Most are based on the expansion of the Earth's gravity field into spherical harmonics; but to make the data usable for ice mass change estimates, it is generally necessary to employ further processing methods. These include the use of averaging kernels (Velicogna et al., 2006), inverse modelling (Wouters et al., 2008; Sasgen et al., 2013), and mass concentration (mascon) approaches (Barletta et al., 2013). Spherical harmonic solutions usually depend on filtering to remove stripes caused by correlated errors (Kusche et al., 2009; Werth et al., 2009).

TCD
8, 2995–3035, 2014

In this paper, we used the latest release of mascon solutions (Luthcke et al., 2013), although we stress that the presented framework is not limited to this class of solutions. The mascon approach employed here directly uses the GRACE K-band inter-satellite range-rate (KBRR) data which are then binned and regularized using smoothness constraints. The release 4 (RL4) Atmosphere/Ocean model correction, which utilizes the European Centre for Medium-Range Weather Forecasts (ECMWF) atmospheric data and the Ocean Model for Circulation and Tides (OMCT), was used (Dobslaw and Thomas, 2007). Some concerns with this correction have been reported (Barletta et al., 2013), but a release of the mascon data using the corrected version (Dobslaw et al., 2013) is not yet available. Contributions to degree-one coefficients were provided using the approach by Swenson et al. (2008). The mascon approach used here does not call for a replacement of C20 coefficients. We assume that GRACE does not observe SMB or ice mass changes over the floating ice shelves as they are in hydrostatic equilibrium. Hence, all observed mass changes over the ice shelves are assumed to be caused by GIA.

Although the mascons are provided at a resolution of about 110 km, their fundamental resolution is very near that of the KBRR data itself (~ 300 km, Luthcke et al., 2013). For the statistical framework, it is important to quantify the correlation among the mascons so that it is taken to account when inferring both the processes and associated uncertainties. We quantify the spatial correlation by determining an averaging model such that the diffused signal is able to loosely reconstruct the mass loss obtained using only altimetry (and assuming that all height change occurs at the density of ice). The averaging strength between mascon neighbours is also estimated during the inference (Zammit-Mangion et al., 2013). The error on the mascon rates is assumed to be a factor of the regression errors, which is also estimated (ibid.).

2.3 GPS

The GPS trends used in this work were taken from Thomas and King (2011). Not all of the trends were suitable for our analysis, as the record length did not always

TCD
8, 2995–3035, 2014

coincide with the 2003–2009 ICESat period. We used stations with contemporaneous data, as well as those where we could access the original time series to confirm that the trend had stayed the same, within the error bounds, for our observation period. For the North Antarctic Peninsula, we followed the approach suggested in the Thomas and King (2011) and used the pre-2003 trends, ignoring the later trend estimates which are highly contaminated by elastic signals. All other stations were corrected for elastic rebound as in Thomas and King (2011) and subsequently assumed to be measuring GIA only (the published rates were used). A more sophisticated approach where the estimated ice loss is fed back into a dynamic estimate of the elastic rebound, is being implemented for a spatiotemporal extension of this work. GPS data used in this study are compiled in Table 1.

2.4 Additional data sets

RACMO: elements of the Regional Atmospheric Climate Model (RACMO, Lenaerts et al., 2012) were used to constrain SMB properties. Spatially-varying length scales describing spatial smoothness of precipitation patterns were obtained from the 2003–2009 SMB anomalies (with respect to the 1979–2002 mean). These ranged from 80 km in the Antarctic Peninsula to 200 km east of Pine Island Glacier. The amplitude of the anomalies, which peaked at 50 mm weq in the Antarctic Peninsula, was used to extract orders of magnitude for expected regional SMB estimates. See Zammit-Mangion et al. (2013) for details. RACMO also provides a surface density map: the mean annual density of the surface layer. This was used to translate height changes corresponding to the SMB field to mass changes.

Firn correction: we used the firn correction anomalies for 2003–2009 (with respect to the 1979–2002 mean) from a firn compaction model (Ligtenberg et al., 2011). These anomalies were used to estimate empirically the correlation between firn compaction rate and surface mass balance. This relationship was then subsequently used to determine jointly the SMB and firn correction processes, subject to the constraint that firn compaction is a linear function of SMB (supported by the high correlation between

TCD
8, 2995–3035, 2014

the respective 2003–2009 trends). The methodology automatically takes into account inflated uncertainties due to confounding of these two processes (since they have identical length scales), see Zammit-Mangion et al. (2013).

Ice Velocities: we use ice velocities derived from Interferometric Synthetic Aperture Radar (InSAR, Rignot, 2011) data. In places where no observational data were available, theoretical balance velocities (Bamber, 2000) were used. Ice velocities were used to help constrain the amount of potential height change which can be attributed to ice dynamics (Sect. 3).

3 Methodology

Our statistical framework makes use of several recent improvements in statistical modelling which can be exploited for geophysical purposes. Details are given in (Zammit-Mangion et al., 2013); here, we only give a brief overview of the approach. The statistical framework hinges on the use of a hierarchical model where the hierarchy consists of three layers, the observation layer (which describes the relation of the observations to the measured fields), the process layer (which contains prior beliefs of the fields using auxiliary data sets) and the parameter layer (where prior beliefs over unknown parameters are described).

The "observation model" is the probabilistic relationship between the observed values and the height change of each of the processes. For point-wise observations, such as altimetry and GPS, the observations were assumed to be measuring the height trend at a specific location. GRACE mascons, on the other hand, were assumed to represent integrated mass change over a given area. These mass changes were translated into height changes via density assumptions: upper mantle density was fixed at 3800 $\mathrm{kg\,m^{-3}}$; ice density at 917 $\mathrm{kg\,m^{-3}}$, and SMB at values ranging from 350–600 $\mathrm{kg\,m^{-3}}$. Recall (Sect. 2.4) that we used the density map from Ligtenberg et al. (2011) to specify the density of the surface layer.

TCD
8, 2995–3035, 2014

In the "process model" four fields are described: ice dynamics, SMB, GIA, and a field which combines the processes which do result in height changes, but no mass changes: firn compaction and elastic rebound. We model the height changes due to these as spatial Gaussian processes, i.e. we assume that they can be fully characterised by a mean function and a covariance function. For each field we assume that the mean function is zero (we do not use numerical models to inform the overall mean) and that the covariance function, which describes how points in space covary, is highly informed by numerical models and expert knowledge as described next.

The practical spatial range of surface processes – this describes the distance beyond which the correlation drops to under 10 % – was estimated from RACMO as described in Sect. 2.4. This analysis revealed, for example, that locations at 100 km are virtually uncorrelated in the Antarctic Peninsula, but highly correlated east of Thwaites. Similarly GIA was found to have a large practical range (∼ 3000 km), from an analysis of the IJ05-R2 model (Ivins et al., 2013). These length scales impose soft restrictions on the possible class of solutions for the individual fields.

Mass loss due to ice dynamics was assumed to mostly take place in areas of high ice velocity (Sasgen et al., 2010) . A "soft" constraint was thus placed on elevation rates due to ice dynamics such that it is small (1 mm yr^{-1}) at areas of low velocities and possibly large (up to 15 m yr^{-1}) at velocities greater than 10 m yr^{-1}. A sigmoid function was used to describe this soft constraint:

$$\sigma_{\text{vel}}(\boldsymbol{s}) = \frac{15}{1 + \exp(-(v(\boldsymbol{s}) - 10))} \tag{2}$$

where $v(\boldsymbol{s})$ denotes the horizontal velocity at location $\boldsymbol{s}$. For illustration of how $\sigma_{\text{vel}}(\boldsymbol{s})$ is used, an altimetry trend of 10 m yr^{-1} in Pine Island Glacier where velocities exceed 4 km yr^{-1} is within the $1\sigma_{\text{vel}}$ interval and thus classified as "probable". On the other hand, a 10 m yr^{-1} trend in a region east of Thwaites, where velocities are 2 m yr^{-1}, would lie within the $2000\sigma_{\text{vel}}$ level and thus assumed to be a virtually impossible occurrence a priori. At Kamb Ice Stream, this assumption had to be altered as this area

TCD
8, 2995–3035, 2014

shows thickening from the stalling of ice stream C 150 years ago (Retzlaff and Bentley, 1993). Although the velocity of the ice is low, the thickening occurs at comparably high rates. To reflect this, we fix $\sigma_{\text{vel}}(\boldsymbol{s}) = 2\,\text{m}\,\text{yr}^{-1}$ in this drainage basin.

Length scales and prior soft constraints are easily defined for Gaussian processes (or Gaussian fields) which, on the other hand, are also computationally challenging to use. Gaussian fields can however be re-expressed as Gaussian Markov Random Fields (GMRF) by recognising that Gaussian fields are in fact solutions to a class of Stochastic Partial Differential Equations (SPDEs, Lindgren et al., 2011). Numerical methods for partial differential equations, namely, finite element (FE) methods, can thus be applied to the SPDEs in order to obtain a computationally efficient formulation of a complex statistical problem.

Spatially varying triangulations (meshes) are used for the different processes reflecting the assumption that, for example, ice loss is more likely to occur on smaller scales on the margins of the ice sheet where fast, narrow ice streams are prevalent, than in the interior. We thus use a fine mesh at the margins (25 km) and a coarse mesh in the interior for this field. GIA on the other hand is a pre-supposed to be smooth. This allows us to use a relatively coarse mesh for this process (~ 100 km).

We note that the methodology differs from others in that it is not a simple average (Shepherd et al., 2012) or sum (Riva et al., 2009) of corrected data sources, but a statistically sound, process-based estimate. For each of the four fields, we infer a probability distribution and standard deviation for every point in space. By relating pre-inference and post-inference variances, it is possible to assess the influence of different kinds of observation at each point on the resulting fields.

4 Results

Inferential results are available for all of the four processes in isolation. In this section we report the results for each of the processes in turn, a discussion of these results is provided in Sect. 5.

TCD
8, 2995–3035, 2014

Ice dynamics: the results for ice dynamics (Fig. 1a) are consistent with prior knowledge of disequilibria in ice dynamics in the West Antarctic Ice Sheet (WAIS), for example, the ice build-up in the Kamb Ice Stream catchment (Retzlaff and Bentley, 1993) and the rapid ice loss in the Amundsen Sea Embayment (ASE, Flament et al., 2012). The strength of the approach is apparent when focusing on the Antarctic Peninsula (Fig. 1b). Due to the relatively narrow, steep terrain, and northern latitude (which affects the across track spacing) satellite altimeter data are sparse, while GRACE data are strongly affected by leakage effects, making it challenging to localise the mass sources and sinks. Without prior instruction, the framework places ice loss maxima at the outlets of several glaciers and ice streams. The result is a high-resolution map of ice mass loss or gain that can be linked to specific catchments. Strong ice loss can be observed on the Northern Peninsula at the Weddell Sea shore, at the former tributaries of the Larsen B ice shelf. The maximum ice loss rate is found in the area around Sjögren Glacier with $-4.7\,\mathrm{m\,yr^{-1}}$. Neighbouring Röhss Glacier, on James Ross Island, has been thinning considerably since the break-up of the Prince Gustav Ice Shelf (Glasser et al., 2011; Davies et al., 2012). This is also reflected in high loss rates. Hektoria and Evans, Gregory Glacier, and glaciers the Philippi Rise also show strong ice mass loss signals, most likely as a result of the collapse of the Larsen B ice shelf (Scambos et al., 2004; Berthier et al., 2012). Other ice loss maxima are found in the region of the Wordie Ice Shelf (see Fig. 8 for reference), Marguerite Bay, and Loubet Coast, which corroborates findings from USGS/BAS airborne and ASTER spaceborne stereo imagery analyses (Kunz et al., 2012). Ice loss is also observed on King George Island, which is in agreement with recent analyses of satellite SAR data (Osmanoğlu et al., 2013), and on Joinville Island. Ice build-up is observed over the Southern Peninsula (Kunz et al., 2012).

The gap in altimeter data around the pole results in spurious estimates for that region and the shaded area, south of 86°, is not considered here. As expected, the marginal standard deviation, or error estimate, (Fig. 2) is lowest in the interior of the WAIS, where sampling density by altimetry is high, and highest on the Peninsula, where data

TCD
8, 2995–3035, 2014

are sparse. Also, steep coastal areas show larger errors, reflecting the dependency of altimeter errors on slope (see Bamber et al., 2005; Brenner et al., 2007).

SMB and firn compaction: Fig. 3 shows the trend of the cumulative SMB anomalies according to RACMO, calculated with respect to the 1979–2010 mean. This corresponds to the signal we are estimating, since we are only considering trends with respect to a balance state. The results we obtain for SMB (Fig. 4) largely differ from those of RACMO (Fig. 3). This holds especially for the Amundsen Sea Sector. Here, RACMO shows an overall positive trend while our estimate shows a localized negative trend inland, which follows the orography. In Fig. 5, we compare our results with ice core trends from Medley et al. (2013) who conclude that, while in phase, RACMO appears to show exaggerated inter-annual variability in the ASE. The shown ice core trend titled "MEDLEY" is the mean of the three 2010 cores PIG2010, THWAITES2010, and DIV2010; the location in the figure is, consequently, the mean of the three cores' coordinates. The trends at the single ice cores were not listed, but we can see qualitative agreement with our negative trend in the area. Burgener et al. (2013) also provide new ice core records for the Amundsen Sea sector (Satellite Era Accumulation Traverse, SEAT) and Fig. 5 shows a comparison with their data. Trends were taken over the full 2003–2009 period; the mean is 1980–2009. The agreement is good for three out of five cores given in the paper. Following Burgener et al. (2013), we exclude SEAT 10-4 because of the high noise level in the isotope dating and surface undulations. SEAT10-5 shows a strong negative trend that cannot be reproduced. SEAT-01, SEAT-03, and SEAT-06 agree well with our results at a centimetre scale. We note, however, that there is relatively large spatial variability in SMB based on the ice core data, not catered for in our framework.

Height changes from firn compaction and elastic rebound are estimated together in one field. Because they take place on similar length scales, and there is no temporal evolution in the time-invariant solution, they are confounded in this study. Since firn compaction occurs at relatively large rates, we cannot make any useful inferences about elastic rebound rates. We expect this issue to be less critical in the

TCD
8, 2995–3035, 2014

time-evolving solution. The modelled inverse correlation between firn compaction and SMB (Sect. 2.4) is visible in the results (Figs. 4 and 6).

GIA: GIA vertical velocities estimated by our framework are considerably lower than many older forward model solutions (e.g. Peltier, 2004; Ivins and James, 2005). Our results, however, agree well with a recent GRACE-derived estimate, AGE-1, which also adopts the assumption that over the ice shelves, GIA is the sole process causing observed mass change (Sasgen et al., 2013). Compared with AGE-1, our maxima in vertical uplift are shifted towards the open ocean for both of the major ice shelves (Fig. 7). Agreement with the trends at most GPS stations is good; however, the imposed smoothness constraints have a larger influence. The W06A station (Table 1), which has a strong negative trend with a large error, exacerbated by a strong elastic signal, stands out. Thomas and King (2011) show that its rate does not fit with any of the GIA models used in their comparison. The signal is effectively ignored in this framework due to the large spatial scale assumed for the GIA process.

In Fig. 9, we compare our results (denoted "RATES") with basin estimates from AGE-1 (Sasgen et al., 2013), two recent forward models, W12a (Whitehouse et al., 2012) and IJ05-R2 (Ivins et al., 2013), and a data-driven inversion by Gunter et al. (2014) (denoted "Gunter14"), which is an update of Riva et al. (2009). Basin definitions are shown in Fig. 8. Both Gunter14 and AGE-1 rely on GRACE data. W12a, while a forward model, was adjusted to better match GPS uplift rates on the Peninsula. Overall, we obtain best agreement with the AGE-1 solution. For the Filchner Ronne Ice Shelf (basin 1), the AGE-1 estimate (2.1 mm yr^{-1}) is slightly lower than ours (2.7 mm yr^{-1}), while IJ05-2 is slightly higher (3.5 mm yr^{-1}). W12a (7.2 mm yr^{-1}) shows more than twice our rate in this area, while Gunter14 (4.2 mm yr^{-1}) lies between IJ05-R2 and W12a. At the Ross Ice Shelf (basin 18), the agreement with AGE-1 and IJ05-R2 (both 1.9 mm yr^{-1}, RATES 2.0 mm yr^{-1}) is very close. Gunter14 (3.1 mm yr^{-1}) and W12a (3.4 mm yr^{-1}) are slightly higher. For basin 19, again the agreement with AGE-1 and IJ05-R2 is close with RATES at 2 mm yr^{-1}, AGE-1 at 1.7 mm yr^{-1} and IJ05-R2 at (1.9 mm yr^{-1}). Gunter14

TCD
8, 2995–3035, 2014

and W12a are, again, somewhat higher here, at 2.6 and 2.7 mm yr^{-1}, respectively. All model estimates lie within our error bounds.

Basin 20 lies between the Ross Ice Shelf region and the Amundsen Sea sector. Here, our uplift rate (1.1 mm yr^{-1}) agrees best with IJ05-2 (0.9 mm yr^{-1}), with AGE-1 at 0.5 mm yr^{-1} and W12a at 1.8 mm yr^{-1}. Gunter14 has the highest rate (2.2 mm yr^{-1}) for this basin. Basins 21 and 22 extend to the Amundsen Seas Sector, one of the most rapidly changing areas in Antarctica. The large volume of ice loss in this area causes large elastic loading responses. Groh et al. (2012) and Gunter et al. (2014) have both mentioned the possibility of a present-day viscoelastic signal in this area. Our uplift estimate for basin 21 is comparably small at 0.6 mm yr^{-1}. AGE-1 (0.7 mm yr^{-1}) is closest to this estimate, while IJ05 (1.6 mm yr^{-1}) and W12a (3.1 mm yr^{-1}) are considerably higher. Gunter14 has the highest rate at 5.4 mm yr^{-1}. In basin 22, again, we agree best with AGE-1 (1.1 mm yr^{-1}, RATES at 0.9 mm yr^{-1}), while all other estimates are higher. Gunter14 and W12a cover the higher end at 4.5 and 4.8 mm yr^{-1} respectively, and IJ05-R2 lies in the middle at 3.0 mm yr^{-1}. Basin 23, which connects the ASE to the Southern Peninsula, also yields a small uplift rate (0.4 mm yr^{-1}). AGE-1 (0.5 mm yr^{-1}) lies within the error estimate, with IJ05-R2 (1.7 mm yr^{-1}) and Gunter14 (2.0 mm yr^{-1}) just outside, and W12a considerably higher at 5 mm yr^{-1}.

On the Southern Peninsula (basin 24), agreement with AGE-1 (1.2 mm yr^{-1}, RATES 1.3 mm yr^{-1}) is very good, but W12a is close (1.8 mm yr^{-1}). Gunter14 and IJ05 both show uplift on the Southern Peninsula, but at a higher rate of 2.4 and 3.1 mm yr^{-1}, respectively. On the Northern Peninsula, again the agreement is best with AGE-1 (0.8 mm yr^{-1}, RATES 0.7 mm yr^{-1}), followed by IJ05-R2 (0.5 mm yr^{-1}). The W12a rate is higher at 1.7 mm yr^{-1}. Gunter14 is the only model that shows a negative GIA trend (−0.70 mm yr^{-1}) in this region.

TCD
8, 2995–3035, 2014

5 Discussion

Figure 10 and Table 2 show the basin-scale combined ice and SMB loss in comparison with two recent studies using GRACE (King et al., 2012; Sasgen et al., 2013). The Sasgen et al. (2013) rates span the ICESat period and were derived for this publication. The King et al. (2012) rates span the 2002–2010 period. Basin definitions are the same as those in Sasgen et al. (2013) (as shown in Fig. 8) but differ from King et al. (2012): the sum of our basins 1 and 24 match the sum of their basins 1, 24 and 27. Our basin 25 matches the sum of their basins 25 and 26. Consequently, comparisons for these basins are not shown in Fig. 10 but provided in Table 2.

Overall, the agreement with Sasgen et al. (2013) is close: we arrive at a mean, time-averaged ice loss rate of $-76 \pm 15\,\mathrm{GT\,yr^{-1}}$, compared with $-87 \pm 10\,\mathrm{GT\,yr^{-1}}$ for Sasgen et al. (2013). Agreement at the basin scale is also good. For Basin 18, our error estimates are inflated because of the pole gap in the altimetry data. The largest differences occur in basins 19, 20 and 23. For 19 and 20, agreement is very good when comparing the sums of the two adjacent basins – indicating that leakage effects might be playing a key role in this discrepancy (due to the particular geometry of the basins). For basin 23, the altimetry – both EnviSat and ICESat – show a clear positive trend in this area (ICESat: $+4\,\mathrm{GT\,yr^{-1}}$), with only very localized ice loss signals on Ferrigno ice stream. This positive trend (as opposed to a negative trend from GRACE) reduces the ice loss estimate and causes the discrepancy. The strong GRACE mass loss signal for the Amundsen Sea sector leads to increased leakage in the coastal basins. The King et al. (2012) result shows basins 23 and 21 are strongly correlated at $p = 0.96$. When comparing the sum over the coastal basins 21, 22, and 23, the difference between the Sasgen et al. (2013) estimate ($-80\,\mathrm{GT\,yr^{-1}}$) and ours ($-74\,\mathrm{GT\,yr^{-1}}$) reduces to just $6\,\mathrm{GT\,yr^{-1}}$.

We also compare our basin scale results to ice loss rates from King et al. (2012). Here, the observation periods do not coincide, and the GIA estimates differ widely. Still, there is reasonable agreement at the basin-scale. Good agreement is observed in

TCD
8, 2995–3035, 2014

basins where their GIA estimates (Whitehouse et al., 2012) lie within our error ranges (basins 18, 19) and worst where their GIA uplift rate is a multiple of ours (sum of basins 1 and 24). Overall, their ice loss rate of $-118 \pm 9\,\mathrm{GT\,yr^{-1}}$ is significantly higher than ours.

Our estimate is lower than other current estimates: Shepherd et al. (2012) arrive at $-97 \pm 20\,\mathrm{GT\,yr^{-1}}$ for WAIS over the ICESat period; while Gunter et al. (2014) obtain $-105 \pm 22\,\mathrm{GT\,yr^{-1}}$. With regards to Shepherd et al. (2012) and other altimetry-based results, the discrepancy is mostly due to our estimate of a negative SMB anomaly in the ASE. RACMO gives a positive signal in this region (Fig. 3). Methodologies employing RACMO will, hence, attribute a greater loss (for a given height change) to ice dynamics. Since these losses occur at a higher density than SMB, the induced mass loss is greater. With regards to Gunter et al. (2014), the discrepancy arises from the different estimated GIA rates in the ASE. One cause for this might be the different GRACE solutions used. Our GRACE data set (Luthcke et al., 2013) is equivalent to a RL04 GRACE solution and uses the same antialiasing products. In Gunter et al. (2014), RL05 GRACE solutions appear to yield higher overall mass loss estimates. Still, preliminary comparisons of new (RL05) mascon solutions with the RL04 ones show little impact on the trends. A study of the influence of the different GRACE solutions, which would encompass different releases and include a comparison between spherical harmonics and mascon solutions is noted as future work.

The results for SMB stand out in this study as they do not agree with those obtained from RACMO (Lenaerts et al., 2011). However, some agreement can be shown with new in situ data from deep ice cores (Medley et al., 2013; Burgener et al., 2013). It should be remarked that in the Amundsen Sea Embayment, where we also observe an ice loss maximum, the statistical framework might have difficulty in separating SMB and ice dynamics. The reason for this is that the density of the SMB changes tends to be higher at the coast, with higher temperatures and melt rates. Some of the large, negative trends seen in the ASE could thus be falsely attributed to SMB. This could be remedied in principle by including more information on the spatial patterns of SMB

TCD
8, 2995–3035, 2014

into our framework by using a more informative prior. Also, it should be noted that the uncertainties on our SMB rates, although low on a basin scale, are comparably high on a small spatial scale. This is in part an intrinsic problem in signal separation, but could be improved by adding in situ data which was used for validation in this analysis.

Methods that combine altimetry and gravimetry such as Gunter et al. (2014) and also this paper are very sensitive to differing SMB estimates. We illustrate this sensitivity in a simple calculation: let the unobserved reality on a $1\,m^2$ unit area be as follows: SMB amounts to $0.2\,m\,yr^{-1}$ at $350\,kg\,m^{-3}$ density; GIA is $1\,mm\,yr^{-1}$ at $3800\,kg\,m^{-3}$; and ice loss is at $-1.0\,m$ at $917\,kg\,m^{-3}$. This amounts to an observed height change of $-0.799\,m\,yr^{-1}$. The observed mass change is $-843.2\,kg\,yr^{-1}$ on the unit m^2. We now try to explain these signals by taking into account GRACE and altimetry, but erroneously assume an SMB rate that is slightly too high – 2 cm higher – at $0.22\,m\,yr^{-1}$ (amounting to a positive mass change of $77\,kg\,yr^{-1}$). The remaining mass signal that needs to be explained by ice and GIA is now $-920.2\,kg\,yr^{-1}$. The unexplained height change is $-1.019\,m$. We arrive at two equations, one for height and one for mass, that can be solved by finding the intersection of the two lines (see Fig. 11). Solving the equations, we arrive at an ice mass loss rate of $-1.024\,m\,yr^{-1}$ with a high, but still plausible GIA rate of $5\,mm\,yr^{-1}$. So overall, a 2 cm difference in SMB can result in a GIA estimate that is considerably higher than the truth. The resulting ice mass difference would be in the range of $-40\,GT$ when taken over the whole of West Antarctica. Naturally, this sensitivity acts both ways, so an underestimate of SMB would result in a lower GIA, and lower ice loss. In this context, both GRACE filtering and the treatment of the ICESat trends also play a major role. As the mass loss signal in this region is very local, with very high rates confined to several kilometres, the inclusion or exclusion of a single (informative) pixel in the altimetry data can alter the height change signal considerably.

The GIA estimates from our study agree very well with a recent GRACE-based estimate (Sasgen et al., 2013) and also compare well to state-of-the-art forward model (Ivins et al., 2013). Compared to AGE-1, the spatial pattern of our uplift maximum is shifted away from the Peninsula and towards the Ronne Ice Shelf. The spatial pattern

TCD
8, 2995–3035, 2014

resembles more the W12a and ICE-5G models, with a bimodal uplift maximum centred underneath the Ronne and Ross Ice Shelves. This spatial structure is likely to have resulted from the use of GPS uplift rates, which were also used in the calibration of the most recent forward models (Whitehouse et al., 2012; Ivins et al., 2013). The W12a model yields slightly higher estimates for most basins but shows good agreement in on the Southern Antarctic Peninsula. Whitehouse et al. (2012) remark that the uplift rates using the W12 de-glaciation history – which are already substantially lower than the ICE-5G (Peltier, 2004) model rates – can be viewed as an upper bound. In this light, our estimates corroborate the general shift in expert opinion in recent years towards a lower GIA uplift rate. However, note that all the above-mentioned GIA estimates share common data – IJ05-R2 uses geological data collated by Whitehouse et al. (2012); which in turn uses the same GPS data (Thomas and King, 2011) that is used by Sasgen et al. (2013) and also in this study. While the lower rates agree better with IJ05-R2 and AGE-1, the spatial pattern of the uplift conforms better with that of W12a, or ICE-5G. It should be remarked that, although we used some common GPS trends which were also employed in the adjustment of W12a, we only used a subset of the Thomas and King (2011) data set because not all time series were available for the 2003–2009 time period at the time of writing (See Table 1, Fig. 7) .

Separating secular and present-day viscous and elastic signals from the trends in this area remains a challenging task and will be treated in greater detail in the spatio-temporal version of our framework. Contrary to Gunter et al. (2014), we do not observe significant uplift in the Amundsen Sea Sector. Although a present-day viscoelastic component in the uplift, resulting from strong ice losses over the past decade, may be possible (Karato, 2008), our preliminary studies show that this uplift would probably not be as pronounced and especially not as widespread as that in Gunter et al. (2014). Rather, we assume that their result stems from an overestimation of SMB rates in the area.

For this proof-of-concept study, our focus lies mainly on ice, SMB and GIA estimates, neglecting to a certain extent the influence of mass-invariant height changes. At this

TCD
8, 2995–3035, 2014

stage, the model only reserves one field for (purely) elastic rebound of the earth's crust and firn compaction. In the time-invariant framework, the two are confounded and cannot be separated, as they are not distinguishable by different densities or length scales. A better way to solve for the elastic rebound of the crust would be to integrate a dynamic estimate that depends on the ice load changes. This approach is being implemented in the spatiotemporal version of the model. The firn compaction is currently linked with SMB through a simple correlation model (Zammit-Mangion et al., 2013). This approach could be further improved by adding a temperature dependence, along the lines of a simple firn compaction model (Helsen et al., 2008). Finally, another open question concerns the extent of present-day viscoelastic rebound in the Amundsen sea sector. The scientific community will have to wait for the official release of the POLENET GPS trends to resolve this issue.

6 Conclusions

The proof-of-concept study shows that hierarchical modelling is a valuable tool in separating ice mass balance, SMB and GIA processes when combining satellite altimetry, GPS and gravimetry. It shows that, using only minimal input from forward models, it can provide an accurate and plausible estimate of the different processes. A time-varying version of the framework is currently being developed, several improvements for which have already been devised. One crucial improvement is the dynamic estimation of elastic rebound in the GPS time series, and the implementation of a dynamic, if simplified firn correction model. One advantage of the framework is that new data – which need be neither regular, nor gridded – can be added at any point. For example, it would be quite easy to extend the observation period to include older or younger data like ERS2, or Cryosat2. Preliminary tests have shown that the inference can also be performed without GRACE data. Another option is to include in situ SMB data that have previously been used for validation.

TCD
8, 2995–3035, 2014

Acknowledgements. The authors would like to thank the following colleagues for helpful discussions: V. Klemann, I. Sasgen, M. King, L. Petrie, P. Clarke, M. Horwath, F. Lindgren and V. Barletta. This work was funded by UK NERC grant NE/I027401/1.

Also, the following colleagues provided additional data without which the project would not have been possible: J. M. Lenaerts, S. Ligtenberg, E. Ivins, R. Riva, B. Gunter, P. Whitehouse, I. Sasgen, R. Bingham, G. Nield and L. Thomas.

References

Arthern, R. J., Vaughan, D. G., Rankin, A. M., Mulvaney, R., and Thomas, E. R.: In situ measurements of Antarctic snow compaction compared with predictions of models, J. Geophys. Res., 115, F03011, doi:10.1029/2009JF001306, 2010.

Bamber, J. and Gomez-Dans, J. L.: The accuracy of digital elevation models of the Antarctic continent, Earth Planet. Sc. Lett., 237, 516–523, 2005.

Bamber, J. L., Vaughan, D. G., and Joughin, I.: Widespread complex flow in the interior of the Antarctic ice sheet, Science, 287, 1248–1250, 2000.

Bamber, J. L., Gomez-Dans, J. L., and Griggs, J. A.: A new 1 km digital elevation model of the Antarctic derived from combined satellite radar and laser data – Part 1: Data and methods, The Cryosphere, 3, 101–111, doi:10.5194/tc-3-101-2009, 2009.

Barletta, V. R., Sørensen, L. S., and Forsberg, R.: Scatter of mass changes estimates at basin scale for Greenland and Antarctica, The Cryosphere, 7, 1411–1432, doi:10.5194/tc-7-1411-2013, 2013.

Berthier, E., Scambos, T. A., and Shuman, C. A.: Mass loss of Larsen B tributary glaciers (Antarctic peninsula) unabated since 2002, Geophys. Res. Lett., 39, L13501, doi:10.1029/2012GL051755, 2012.

Borsa, A. A., Moholdt, G., Fricker, H. A., and Brunt, K. M.: A range correction for ICESat and its potential impact on ice-sheet mass balance studies, The Cryosphere, 8, 345–357, doi:10.5194/tc-8-345-2014, 2014.

Brenner, A. C., DiMarzio, J. P., and Zwally, H. J.: Precision and accuracy of satellite radar and laser altimeter data over the continental ice sheets, IEEE T. Geosci. Remote, 45, 321–331, 2007.

TCD

8, 2995–3035, 2014

Burgener, L., Rupper, S., Koenig, L., Forster, R., Christensen, W. F., Williams, J., Koutnik, M., Miège, C., Steig, E. J., Tingey, D., Keeler, D., and Riley, L.: An observed negative trend in West Antarctic accumulation rates from 1975 to 2010: evidence from new observed and simulated records, J. Geophys. Res.-Atmos., 118, 1–12, doi:10.1002/jgrd.50362, 2013.

Chen, J. L., Wilson, C. R., Blankenship, D. D., and Tapley, B. D.: Antarctic mass rates from GRACE, Geophys. Res. Lett., 33, L11502, doi:10.1029/2006GL026369, 2006.

Danesi, S. and Morelli, A.: Structure of the upper mantle under the Antarctic Plate from surface wave tomography, Geophys. Res. Lett., 28, 4395–4398, 2001.

Davies, B. J., Carrivick, J. L., Glasser, N. F., Hambrey, M. J., and Smellie, J. L.: Variable glacier response to atmospheric warming, northern Antarctic Peninsula, 1988–2009, The Cryosphere, 6, 1031–1048, doi:10.5194/tc-6-1031-2012, 2012.

Dee, D. P., Uppala, S. M., Simmons, A. J., Berrisford, P., Poli, P., Kobayashi, S., Andrae, U., Balmaseda, M. A., Balsamo, G., Bauer, P., Bechtold, P., Beljaars, A. C. M., van de Berg, L., Bidlot, J., Bormann, N., Delsol, C., Dragani, R., Fuentes, M., Geer, A. J., Haimberger, L., Healy, S. B., Hersbach, H., Hólm, E. V., Isaksen, L., Kållberg, P., Köhler, M., Matricardi, M., McNally, A. P., Monge-Sanz, B. M., Morcrette, J.-J., Park, B.-K., Peubey, C., Rosnay, P. de, Tavolato, C., Thépaut, J.-N., and Vitart, F: The ERA-interim reanalysis: configuration and performance of the data assimilation system, Q. J. Roy. Meteor. Soc., 137, 553–597, 2011.

Dobslaw, H. and Thomas, M.: Simulation and observation of global ocean mass anomalies, J. Geophys. Res.-Oceans, 112, C05040, doi:10.1029/2006JC004035, 2007.

Dobslaw, H., Flechtner, F., Bergmann-Wolf, I., Dahle, C., Dill, R., Esselborn, S., and Thomas, M.: Simulating high-frequency atmosphere-ocean mass variability for dealiasing of satellite gravity observations: AOD1B RL05, J. Geophys. Res.-Oceans, 118, 3704–3711, 2013.

Flament, T. and Rémy, F.: Dynamic thinning of Antarctic glaciers from along-track repeat radar altimetry, J. Glaciol., 58, 830–840, 2012.

Fretwell, P., Pritchard, H. D., Vaughan, D. G., Bamber, J. L., Barrand, N. E., Bell, R., Bianchi, C., Bingham, R. G., Blankenship, D. D., Casassa, G., Catania, G., Callens, D., Conway, H., Cook, A. J., Corr, H. F. J., Damaske, D., Damm, V., Ferraccioli, F., Forsberg, R., Fujita, S., Gim, Y., Gogineni, P., Griggs, J. A., Hindmarsh, R. C. A., Holmlund, P., Holt, J. W., Jacobel, R. W., Jenkins, A., Jokat, W., Jordan, T., King, E. C., Kohler, J., Krabill, W., Riger-Kusk, M., Langley, K. A., Leitchenkov, G., Leuschen, C., Luyendyk, B. P., Matsuoka, K., Mouginot, J., Nitsche, F. O., Nogi, Y., Nost, O. A., Popov, S. V., Rignot, E., Rippin, D. M.,

TCD
8, 2995–3035, 2014

Rivera, A., Roberts, J., Ross, N., Siegert, M. J., Smith, A. M., Steinhage, D., Studinger, M., Sun, B., Tinto, B. K., Welch, B. C., Wilson, D., Young, D. A., Xiangbin, C., and Zirizzotti, A.: Bedmap2: improved ice bed, surface and thickness datasets for Antarctica, The Cryosphere, 7, 375–393, doi:10.5194/tc-7-375-2013, 2013.

Frezzotti, M., Scarchilli, C., Becagli, S., Proposito, M., and Urbini, S.: A synthesis of the Antarctic surface mass balance during the last 800 yr, The Cryosphere, 7, 303–319, doi:10.5194/tc-7-303-2013, 2013.

Glasser, N. F., Scambos, T. A., Bohlander, J., Truffer, M., Pettit, E., and Davies, B. J.: From ice-shelf tributary to tidewater glacier: Continued rapid recession, acceleration and thinning of Rohss Glacier following the 1995 collapse of the Prince Gustav Ice Shelf, Antarctic Peninsula, J. Glaciol., 57, 397–406, 2011.

Groh, A., Ewert, H., Scheinert, M., Fritsche, M., Rülke, A., Richter, A., and Dietrich, R.: An investigation of glacial isostatic adjustment over the Amundsen Sea Sector, West Antarctica, Global Planet. Change, 98, 45–53, 2012.

Gunter, B. C., Didova, O., Riva, R. E. M., Ligtenberg, S. R. M., Lenaerts, J. T. M., King, M. A., van den Broeke, M. R., and Urban, T.: Empirical estimation of present-day Antarctic glacial isostatic adjustment and ice mass change, The Cryosphere, 8, 743–760, doi:10.5194/tc-8-743-2014, 2014.

Helsen, M. M., van den Broeke, M. R., van de Wal, R. S., van de Berg, W. J., van Meijgaard, E., Davis, C. H., Goodwin, I.: Elevation changes in Antarctica mainly determined by accumulation variability, Science, 320, 1626–1629, 2008.

Hofton, M. A., Luthcke, S. B., and Blair, J. B.: Estimation of ICESat intercampaign elevation biases from comparison of lidar data in East Antarctica, Geophys. Res. Lett., 40, 5698–5703, 2013.

Howat, I. M., Joughin, I., Fahnestock, M., Smith, B. E., and Scambos, T. A.: Synchronous retreat and acceleration of southeast Greenland outlet glaciers 2000–06: Ice dynamics and coupling to climate, J. Glaciol., 54, 646–660, 2008.

Ivins, E. R. and James, T. S.: Antarctic glacial isostatic adjustment: a new assessment, Antarct. Sci., 17, 541–553, 2005.

Ivins, E. R., James, T. S., Wahr, J., Schrama, O., Ernst, J., Landerer, F. W., and Simon, K. M.: Antarctic contribution to sea level rise observed by GRACE with improved GIA correction, J. Geophys. Res.-Earth, 118, 3126–3141, 2013.

TCD
8, 2995–3035, 2014

Karato, S.: Deformation of Earth Materials: an Introduction to the Rheology of Solid Earth, Cambridge University Press, Karato, New York, 2008.
King, M. A., Bingham, R. J., Moore, P., Whitehouse, P. L., Bentley, M. J., and Milne, G. A.: Lower satellite-gravimetry estimates of Antarctic sea-level contribution, Nature, 491, 586–589, 2012.
Kunz, M., King, M. A., Mills, J. P., Miller, P. E., Fox, A. J., Vaughan, D. G., and Marsh, S. H.: Multi-decadal glacier surface lowering in the Antarctic peninsula, Geophys. Res. Lett., 39, L19502, doi:10.1029/2012GL052823, 2012.
Kusche, J., Schmidt, R., Petrovic, S., and Rietbroek, R.: Decorrelated GRACE time-variable gravity solutions by GFZ, and their validation using a hydrological model, J. Geodesy, 83, 903–913, 2009.
Lenaerts, J. T. M., den Broeke, M. R., Berg, W. J., Meijgaard, E. V., and Kuipers Munneke, P.: A new, high-resolution surface mass balance map of Antarctica (1979–2010) based on regional atmospheric climate modeling, Geophys. Res. Lett., 39, L04501, doi:10.1029/2011GL050713, 2012.
Ligtenberg, S. R. M., Helsen, M. M., and van den Broeke, M. R.: An improved semi-empirical model for the densification of Antarctic firn, The Cryosphere, 5, 809–819, doi:10.5194/tc-5-809-2011, 2011.
Lindgren, F., Rue, H., and Lindström, J.: An explicit link between Gaussian fields and Gaussian Markov random fields: the stochastic partial differential equation approach, J. Roy. Stat. Soc. B, 73, 423–498, 2011.
Luthcke, S. B., Sabaka, T. J., Loomis, B. D., Arendt, A. A., McCarthy, J. J, and Camp, J.: Antarctica, Greenland and Gulf of Alaska land-ice evolution from an iterated GRACE global mascon solution, J. Glaciol., 59, 613–631, 2013.
Medley, B., Joughin, I., Das, S. B., Steig, E. J., Conway, H., Gogineni, S., Criscitiello, A. S., McConnell, J. R., Smith, B. E., van den Broeke, M. R., Lenaerts, J. T. M., Bromwich, D. H., and Nicolas, J. P.: Airborne-radar and ice-core observations of annual snow accumulation over Thwaites Glacier, West Antarctica confirm the spatiotemporal variability of global and regional atmospheric models, Geophys. Res. Lett., 40, 3649–3654, 2013.
Moholdt, G., Nuth, C., Hagen, J. O., and Kohler, J.: Recent elevation changes of Svalbard glaciers derived from ICESat laser altimetry, Remote Sens. Environ., 114, 2756–2767, 2010.
Osmanoglu, B., Braun, M., Hock, R., and Navarro, F. J.: Surface velocity and ice discharge of the ice cap on King George Island, Antarctica, Ann. Glaciol., 54, 111–119, 2013.

TCD
8, 2995–3035, 2014

Peltier, W. R.: Global glacial isostasy and the surface of the ice-age Earth: the ICE-5G (VM2) model and GRACE, Annu. Rev. Earth Pl. Sc., 32, 111–149, 2004.
Retzlaff, R. and Bentley, C. R.: Timing of stagnation of Ice Stream C, West Antarctica, from short-pulse radar studies of buried surface crevasses, J. Glaciol., 39, 553–561, 1993.
Rignot, E., Velicogna, I., Van den Broeke, M. R., Monaghan, A., and Lenaerts, J. T. M.: Acceleration of the contribution of the Greenland and Antarctic ice sheets to sea level rise, Geophys. Res. Lett., 38, L05503, doi:10.1029/2011GL046583, 2011.
Riva, R. E., Gunter, B. C., Urban, T. J., Vermeersen, B. L., Lindenbergh, R. C., Helsen, M. M., Bamer, J. L., van der Wal, R. S. W., van den Broeke, M., and Schutz, B. E.: Glacial isostatic adjustment over Antarctica from combined ICESat and GRACE satellite data, Earth Planet. Sc. Lett., 288, 516–523, 2009.
Sasgen, I., Martinec, Z., and Bamber, J.: Combined GRACE and InSAR estimate of West Antarctic ice mass loss, J. Geophys. Res.-Earth, 115, F04010, doi:10.1029/2009JF001525, 2010.
Sasgen, I., Konrad, H., Ivins, E. R., Van den Broeke, M. R., Bamber, J. L., Martinec, Z., and Klemann, V.: Antarctic ice-mass balance 2003 to 2012: regional reanalysis of GRACE satellite gravimetry measurements with improved estimate of glacial-isostatic adjustment based on GPS uplift rates, The Cryosphere, 7, 1499–1512, doi:10.5194/tc-7-1499-2013, 2013.
Scambos, T. A., Bohlander, J. A., Shuman, C. U., and Skvarca, P.: Glacier acceleration and thinning after ice shelf collapse in the Larsen B embayment, Antarctica, Geophys. Res. Lett., 31, L18402, doi:10.1029/2004GL020670, 2004.
Shepherd, A., Ivins, E. R., Geruo, A, Barletta, V. R., Bentley, M. J., Bettadpur, S., Briggs, K. H., Bromwich, D. H., Forsberg, R., Galin, N., Horwath, M., Jacobs, S., Joughin, I., King, M. A., Lenaerts, J. T. M., Li, J., Ligtenberg, S. R. M., Luckman, A., Luthcke, S. B., McMillan, M., Meister, R., Milne, G., Mouginot, J., Muir, A., Nicolas, J. P., Paden, J. , Payne, A. J., Pritchard, H., Rignot, E., Rott, H., Sørensen, L. S., Scambos, T. A., Scheuchl, B., Schrama, E. J. O., Smith, B., Sundal, A. V., van Angelen, J. H., van de Berg, W. J., van den Broeke, M. R., Vaughan, D. G., Velicogna, I., Wahr, J., Whitehouse, P. L., Wingham, D. J., Yi, D., Young, D., and Zwally, H. J.: A reconciled estimate of ice-sheet mass balance, Science, 338, 1183–1189, 2012.
Sørensen, L. S., Simonsen, S. B., Nielsen, K., Lucas-Picher, P., Spada, G., Adalgeirsdottir, G., Forsberg, R., and Hvidberg, C. S.: Mass balance of the Greenland ice sheet (2003–2008)

TCD
8, 2995–3035, 2014

from ICESat data – the impact of interpolation, sampling and firn density, The Cryosphere, 5, 173–186, doi:10.5194/tc-5-173-2011, 2011.
Swenson, S., Chambers, D., and Wahr, J.: Estimating geocenter variations from a combination of GRACE and ocean model output, J. Geophys. Res.-Earth, 113, B08410, doi:10.1029/2007JB005338, 2008.
Tapley, B. D., Bettadpur, S., Ries, J. C., Thompson, P. F., and Watkins, M. M.: GRACE measurements of mass variability in the Earth system, Science, 305, 503–505, 2004.
Thomas, R., Davis, C., Frederick, E., Krabill, W., Li, Y., Manizade, S., and Martin, C.: A comparison of Greenland ice-sheet volume changes derived from altimetry measurements, J. Glaciol., 54, 203–212, 2008.
Thomas, I. D., King, M. A., Bentley, M. J., Whitehouse, P. L., Penna, N. T., Williams, S. D., Riva, R. E. M., Lavallee, D. A., Clarke, P. J., King, E. C., Hindmarsh, E. C. A., and Koivula, H.: Widespread low rates of Antarctic glacial isostatic adjustment revealed by GPS observations, Geophys. Res. Lett., 38, L22302, doi:10.1029/2011GL049277, 2011.
Van de Berg, W. J., van den Broeke, M. R., van Meijgaard, E., and Reijmer, C. H.: Reassessment of the Antarctic surface mass balance using calibrated output of a regional atmospheric climate model, J. Geophys. Res ., 111, D11104, doi:10.1029/2005JD006495, 2006.
Velicogna, I. and Wahr, J.: Measurements of time-variable gravity show mass loss in Antarctica, Science, 311, 1754–1756, 2006.
Werth, S., Güntner, A., Schmidt, R., and Kusche, J.: Evaluation of GRACE filter tools from a hydrological perspective, Geophys. J. Int., 179, 1499–1515, 2009.
Whitehouse, P. L., Bentley, M. J., Milne, G. A., King, M. A., and Thomas, I. D.: A new glacial isostatic adjustment model for Antarctica: calibrated and tested using observations of relative sea-level change and present-day uplift rates, Geophys. J. Int., 190, 1464–1482, 2012.
Wouters, B., Chambers, D., and Schrama, E. J. O.: GRACE observes small-scale mass loss in Greenland, Geophys. Res. Lett., 35, L20501, doi:10.1029/2008GL034816, 2008.
Yan, X.: Linear Regression Analysis: Theory and Computing, World Scientific, Yan, Singapore, 2009.
Zammit-Mangion, A., Rougier, J., Bamber, J., and Schon, N. W.: Resolving the Antarctic contribution to sea-level rise: a hierarchical modelling framework, Environmetrics, 25, 245–264, doi:10.1002/env.2247, 2013.
Zwally, H. J. and Brenner, A. C.: Ice sheet dynamics and mass balance, Int. Geophys., 69, 351–369, 2001.

TCD
8, 2995–3035, 2014

Zwally, H., Schutz, R., Bentley, C., Bufton, J., Herring, T., Minster, J., Spinhirne, J., and Thomas, R.: GLAS/ICESat L2 Antarctic and Greenland Ice Sheet Altimetry Data, Version 33, National Snow and Ice Data Center, Boulder, CO, USA, 2011.

TCD
8, 2995–3035, 2014

Table 1. GPS stations as adapted from Thomas et al. (2011) with vertical rate and errors, modelled elastic correction and adjusted rates. The latter are used for inference.

Site name	Lat	Lon	Start year	Start day of year	End year	End day of year	Data days	GPS rate (mm yr^{-1})	Sigma	Modelled elastic	Adjusted GPS
ABOA	−73.04	346.59	2003	31	2010	11	1959	1.4	0.84	0.27	1.13
BELG	−77.86	325.38	1998	33	2005	45	1517	2.97	1.47	0.02	2.95
BREN	−72.67	296.97	2006	362	2010	194	463	3.85	1.6	1.85	2
FOS1	−71.31	291.68	1995	35	2010	364	317	2.14	0.4	1.64	0.5
MBL1_AV	−78.03	204.98						3.28	1.09	0.28	3
OHIG	−63.32	302.1	1995	69	2002	48	1667	3.8	1	NULL	3.8
PALM	−64.78	295.95	1998	188	2002	59	1181	0.08	1.87	NULL	0.08
ROTB	−67.57	291.87	1999	54	2002	59	239	1.5	1.9	NULL	1.5
SMRT	−68.12	292.9	1999	112	2002	59	751	−0.22	1.93	NULL	−0.22
SVEA	−74.58	348.78	2004	317	2008	20	1030	2.07	1.95	0.24	1.83
VESL	−71.67	357.16	1998	212	2010	328	3081	1.06	0.45	0.25	0.81
W01_AV	−87.42	210.57						−2.8	1.17	−0.09	−2.71
W02_AV	−85.61	291.45						2.17	1	0.28	1.89
W03_AV	−81.58	331.6						−2.47	1.28	−1.73	−0.74
W04_AV	−82.86	306.8						3.42	0.84	0.16	3.26
W04B/CRDI	−82.86	306.8	2002	358	2008	24	16	4.06	1.32	0.16	3.9
W06A	−79.63	268.72	2002	356	2005	358	12	−2.2	2.42	1.53	−3.73
W07_AV	−80.32	278.57						3.61	1.58	0.97	2.64
W09	−82.68	255.61	2003	9	2006	8	34	4.54	2.59	0.49	4.05
W12A/PATN	−78.03	204.98	2003	331	2007	363	17	6.41	1.61	0.28	6.13
W08A/B/SUGG	−75.28	287.82	2003	3	2006	4	13	1.31	1.28	1.3	0.01

TCD
8, 2995–3035, 2014

Table 2. Ice and SMB mass trends from RATES, Sasgen et al. (2013) and King et al. (2012), in GT yr^{-1}.

Basin	RATES Feb 2003–Oct 2009	Sasgen (2013) Feb 2003–Oct 2009	King (2012) 2002–2010	Diff RATES – Sasgen	Diff RATES – King
1	7.6	11	–	−3.4	–
18	16.2	9.5	19.2	6.7	−3
19	−2.2	10	−4	−12.2	1.8
20	−12.2	−23	−23	10.8	10.8
21	−49.5	−46	−54	−3.5	4.5
22	−27.6	−24	−24	−3.6	−3.6
23	2.7	−11	−7	13.7	9.7
24	13.6	12	–	1.6	–
25 (25 + 26)*	−24.1	−25	−33	0.9	8.9
(1 + 24 + 27)*	21.2	23	8.5	−1.8	12.7
WAIS	−75.5	−86.5	−117.3	9.2	41.8

* Our basin 25 is equal to the sum of basins 25 and 26 in King et al. (2012). The sum of our basins 1 and 24 is equal to their sum of basins 1, 24, and 27.

TCD
8, 2995–3035, 2014

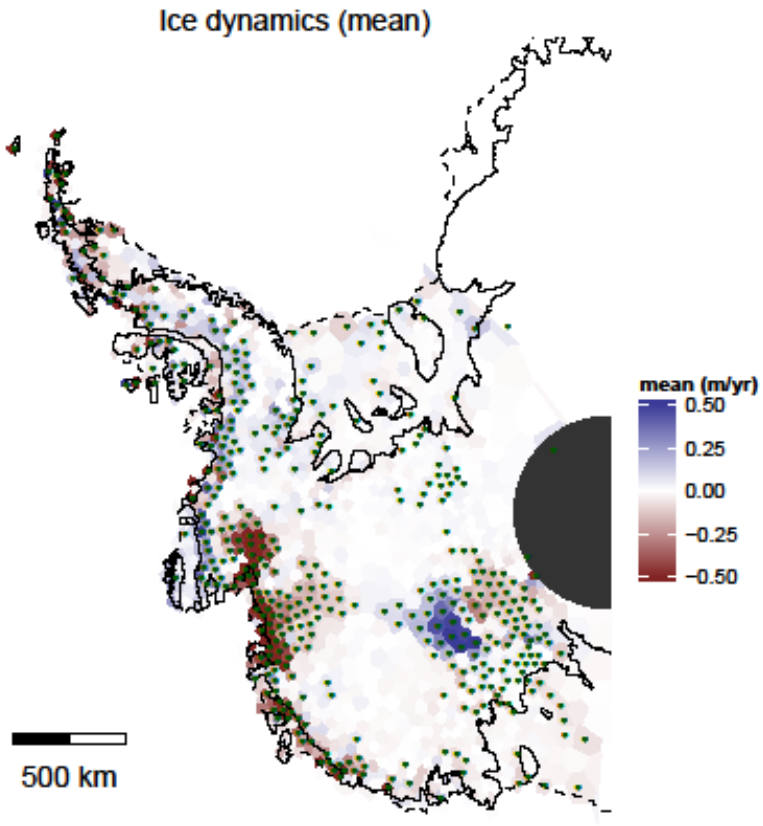

Figure 1a. Ice dynamics for 2003–2009 in $m\,yr^{-1}$. Stippled points denote areas in which the mean signal is larger than the marginal standard deviation.

TCD
8, 2995–3035, 2014

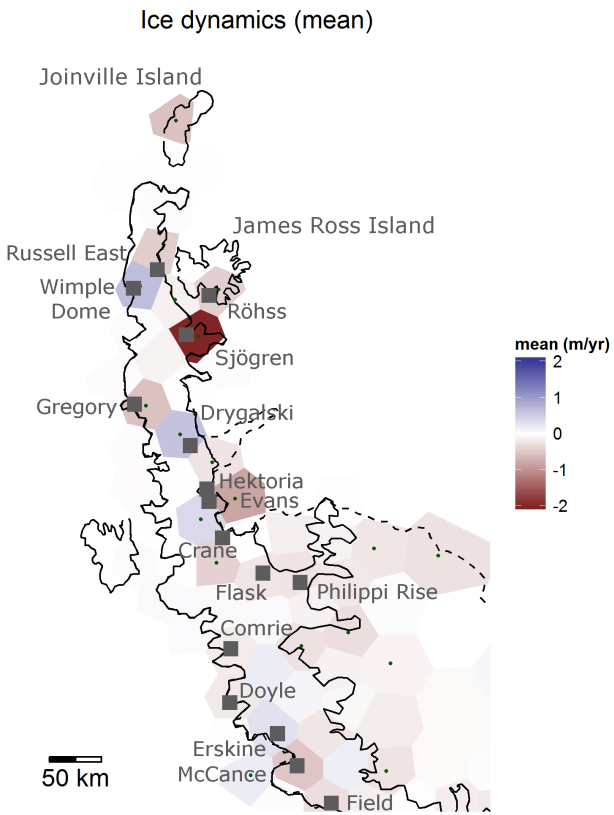

Figure 1b. Ice dynamics for 2003–2009 in $\mathrm{m\,yr^{-1}}$. Close-up for the Northern Antarctic Peninsula, with glacier locations (grey squares). Stippled points denote areas in which the mean signal is larger than the marginal standard deviation.

TCD
8, 2995–3035, 2014

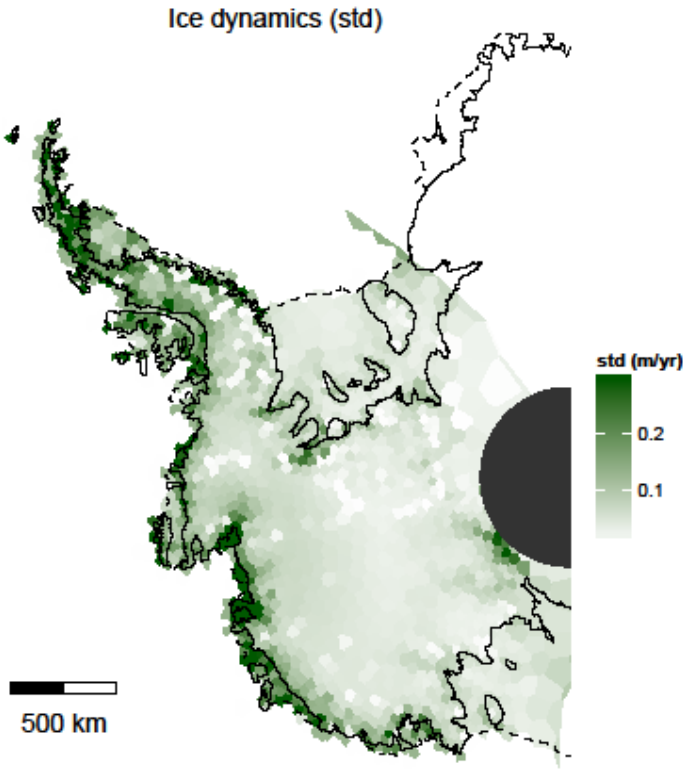

Figure 2. Marginal standard deviation of ice dynamics for 2003–2009 in m yr^{-1}.

TCD
8, 2995–3035, 2014

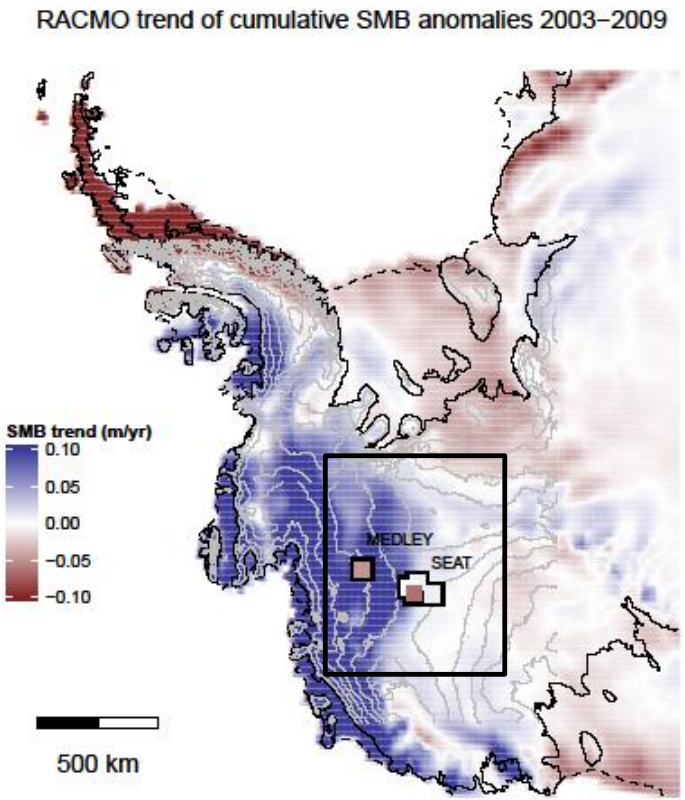

Figure 3. The SMB trend for 2003–2009 as obtained from RACMO. Contour lines (shown from −1000 to 1000 km Northing) are elevations from BEDMAP surface (Fretwell et al., 2013). Mean ice core accumulation rates from Medley et al. (2013) (denoted MEDLEY) and ice core accumulation rates from Burgener et al. (2013) (denoted SEAT). Rectangle shows area in close-up (Fig. 5).

TCD
8, 2995–3035, 2014

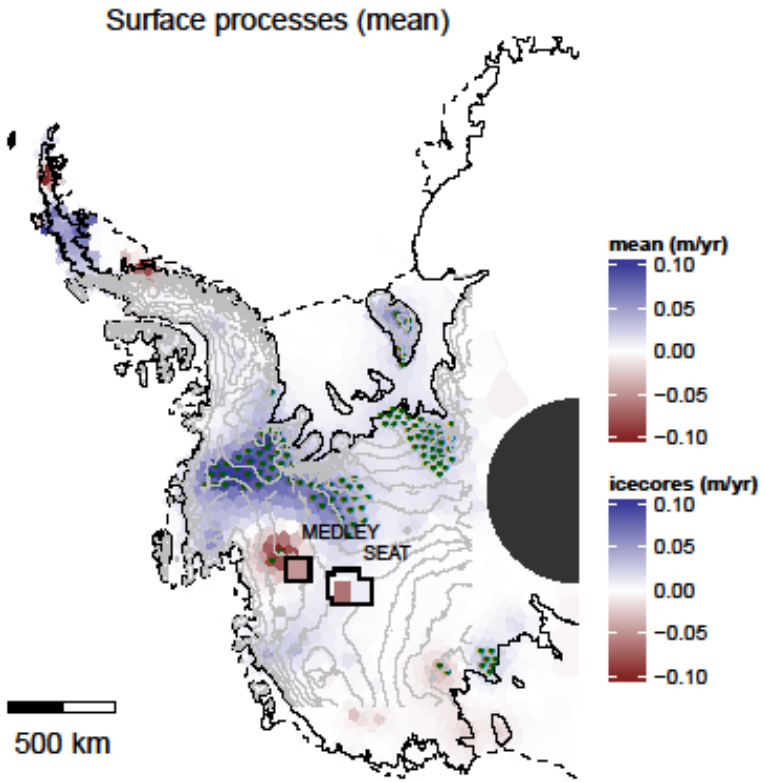

Figure 4. SMB rates for 2003–2009 in m yr^{-1} and locations of the ice cores from Burgener et al. (2013) and Medley et al. (2013). Contour lines (shown from −1000 to 1000 km Northing) are elevations from BEDMAP surface (Fretwell et al., 2013). Stippled points denote areas in which the mean signal is larger than the marginal standard deviation.

TCD
8, 2995–3035, 2014

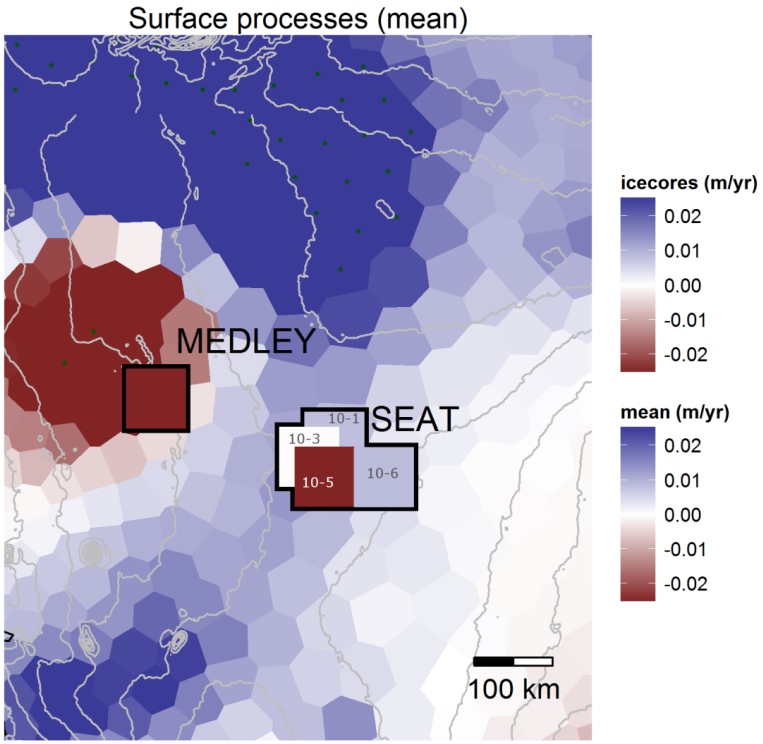

Figure 5. Close-up of ice core mean from Medley et al. (2013) (denoted MEDLEY) and ice cores from Burgener et al. (2013) and RATES SMB trends for 2003–2009 in the Amundsen Sea Embayment. Numbers denote SEAT ice cores 10-1, 10-3, 10-5, and 10-6. Contour lines are elevations from BEDMAP surface (Fretwell et al., 2013). Stippled points denote areas in which the mean signal is larger than the marginal standard deviation.

TCD
8, 2995–3035, 2014

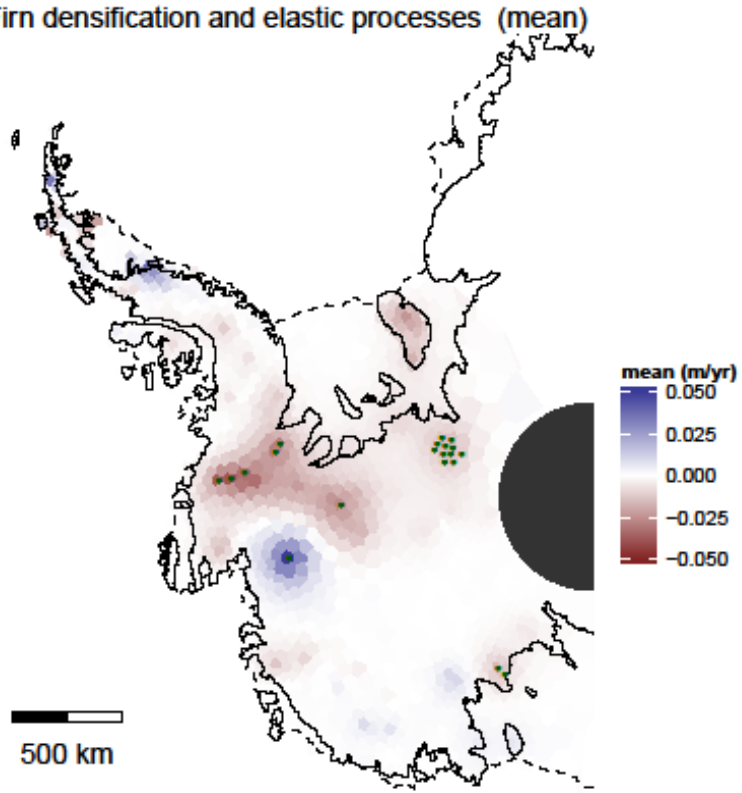

Figure 6. Height changes from firn compaction and elastic uplift of the crust for 2003–2009 in m yr^{-1}. Stippled points denote areas in which the mean signal is larger than the marginal standard deviation.

TCD
8, 2995–3035, 2014

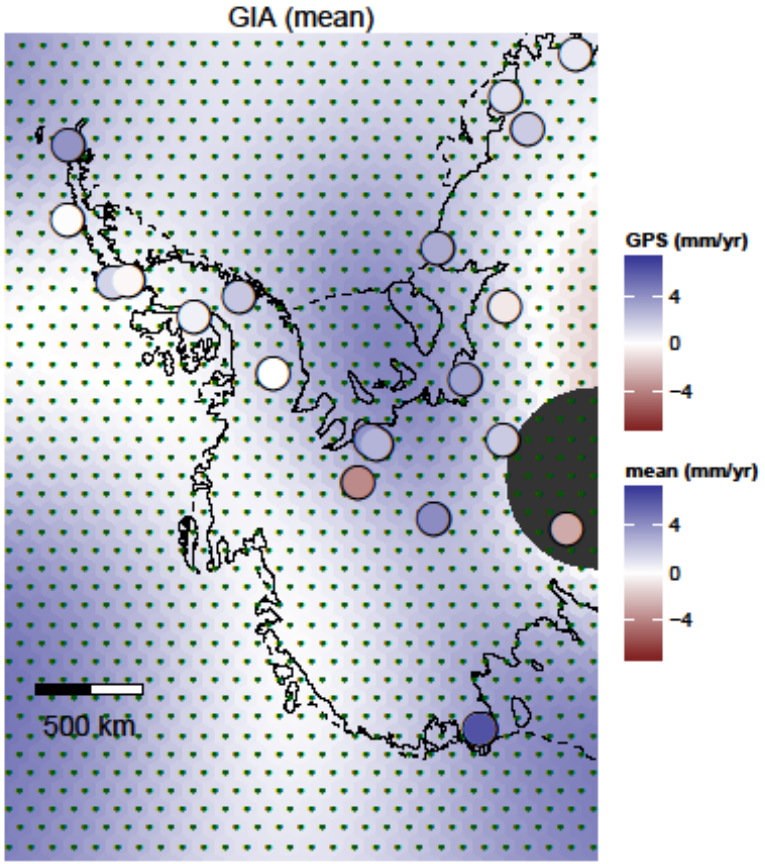

Figure 7. GIA estimate with GPS stations and their rates. Stippled points denote areas in which the mean signal is larger than the marginal standard deviation.

TCD
8, 2995–3035, 2014

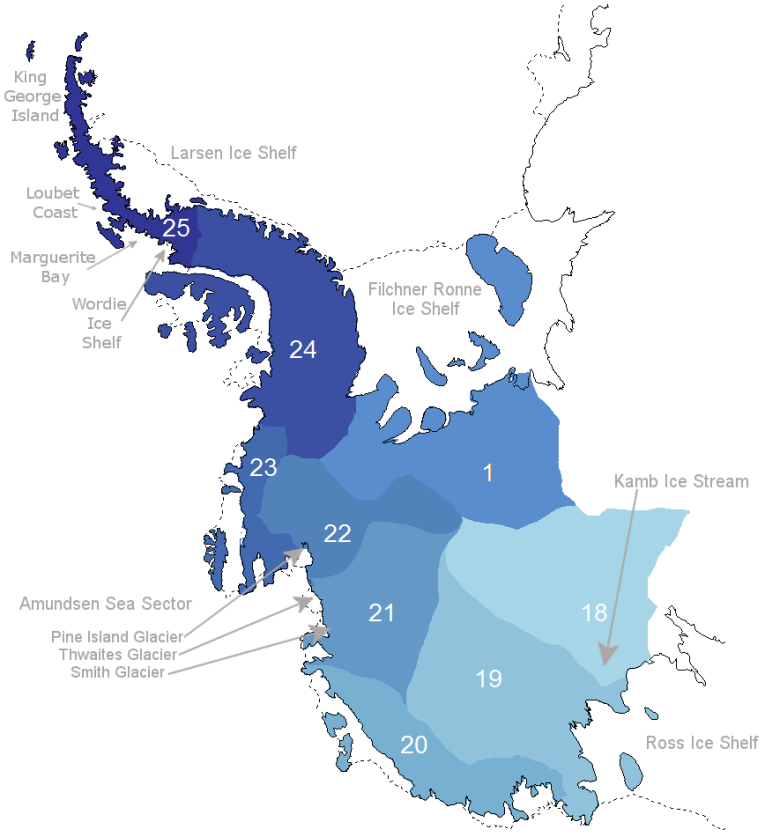

Figure 8. Basin definitions used for West Antarctica (adapted from Sasgen et al., 2013).

TCD
8, 2995–3035, 2014

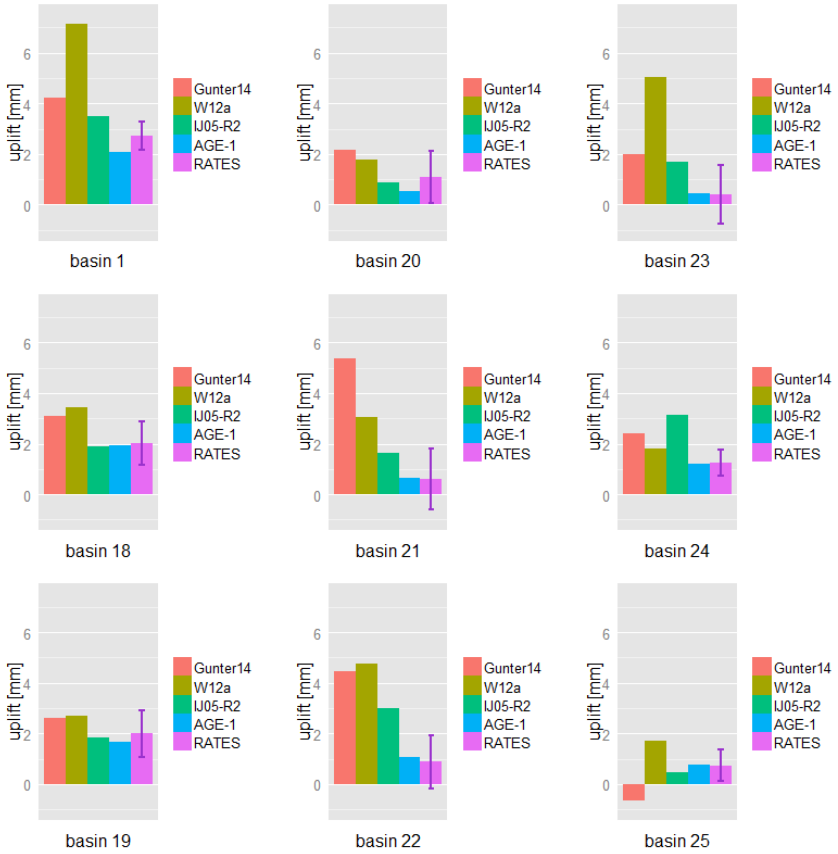

Figure 9. Comparison of RATES results with different GIA estimates and forward models.

TCD
8, 2995–3035, 2014

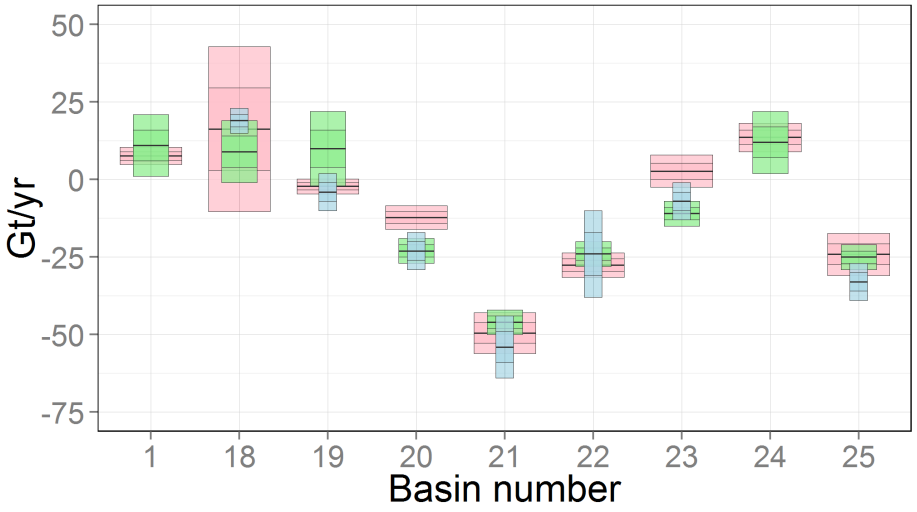

Figure 10. Combined ice and SMB loss trends for West Antarctica using RATES (pink), results from King et al. (2013) (blue), and from Sasgen et al. (2013) (green). Basin definitions for King et al. (2012) differ for basins 1 and 24, so they are given in Table 2 instead. Our basin 25 is equal to the sum of basins 25 and 26 in King et al. (2012), this is given here as basin 25 for the King estimate.

TCD
8, 2995–3035, 2014

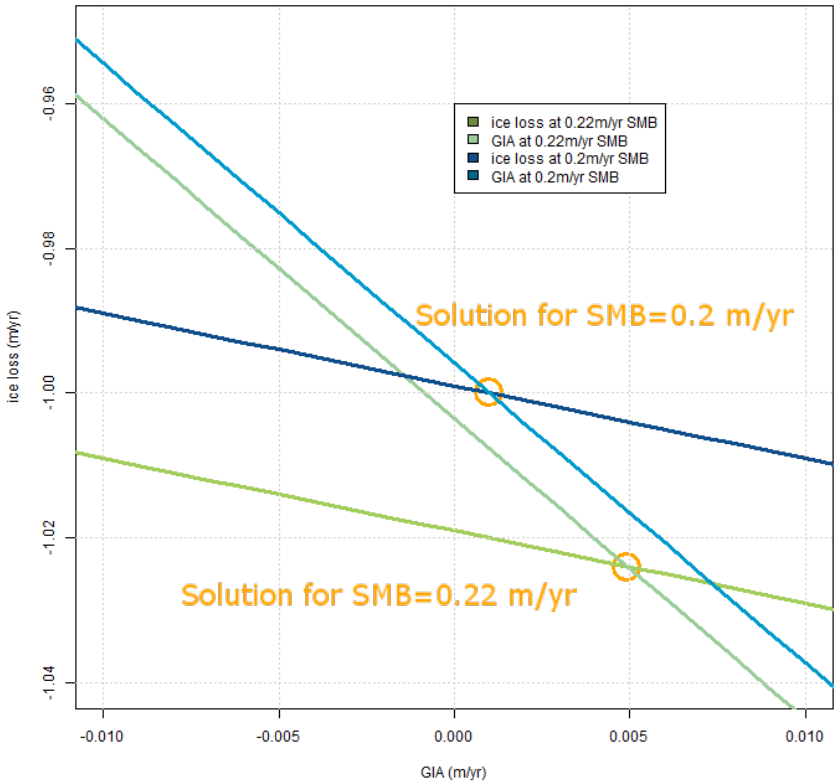

Figure 11. Toy example illustrating the sensitivity of combination methods to differing SMB estimates. The blue lines represent the set of equations that solve for ice loss and GIA when SMB = 0.2 m yr^{-1}. The green lines represent the equations for SMB = 0.22 m yr^{-1}.

TCD
8, 2995–3035, 2014